(Received 22 April 2024, Accepted 6 June 2024, Scheduled 19 June 2024)

Improved Target Imaging Method for Arc Array Bistatic SAR with a Small Satellite Transmitter

Peigeng Lu[1,2], Zhennan Qin[1,2], Wei Xu[1,2,*], Pingping Huang[1,2], Weixian Tan[1,2], and Yaolong Qi[1,2]

[1] *Inner Mongolia Key Laboratory of Radar Technology and Application, Hohhot 010051, Inner Mongolia, China*
[2] *College of Information Engineering, Inner Mongolia University of Technology, Hohhot 010051, Inner Mongolia, China*

ABSTRACT: Modern small satellite development represents a new trend, a new design idea, and it can be used as a transmitter to assist helicopter monitoring. The imaging model of the arc array bistatic SAR with a small satellite transmitter is studied. Due to the long resident time of small satellite platform and the wide-area observation capability of arc antenna, it has a wide application prospect in the field of earth detection and remote sensing. However, the motion state of the small satellite and the special scanning mode of the arc antenna have some effects on the SAR imaging results. Therefore, the imaging geometry of the arc array bistatic SAR with a small satellite transmitter is established, and an improved Chirp Scaling imaging algorithm is proposed. Firstly, the motion compensation function is used to compensate the migration caused by the high-speed motion of the small satellite. Then, the two-dimensional spectrum is derived by using standing phase principle and scaling function. Next, the coupling between range and azimuth is compensated by consistent range migration correction and secondary range compression, and residual phase is compensated in azimuth frequency domain. Finally, simulation results verify the effectiveness of the proposed method.

1. INTRODUCTION

In recent years, the number of small satellites launched has increased dramatically, becoming the main driving force for the rapid development of global space activities [1]. Many small satellites often form a constellation network in the form of a distributed space system, replacing a single medium and high orbit large satellite, and even providing better technical performance. Small satellites have many advantages, such as low cost, easy launch, emergency capability and flexibility, and short system construction cycle. They provide low-cost solutions for special communication, remote sensing, technical experiments, and earth observation, and their application prospects are very broad [2].

Modern small satellites are in the popular space era, and the failure of a single small satellite cannot seriously affect the performance of a constellation network system. This makes the small satellite a reliable source of transmitter, which is expected to cooperate with other small satellites, aircraft, etc., to improve various application scenarios. In actual operation, helicopters can coordinate work with small satellites in the space field, and several small satellites can act as transmitters to assist work, showing the great potential of multi-field cooperation. Therefore, an imaging model of arc array bistatic synthetic aperture radar (AA-BiSAR) with the small satellite transmitter is proposed, which combines modern small satellite and airborne arc array SAR [3, 4], and has the advantages of both, including global real-time observation, 360° omni-directional coverage, and strong anti-interference ability [5, 6]. This model has a wide application prospect in the field of Earth observation and remote sensing, and further promotes the development of small satellites in multi-field collaborative work.

In recent years, many studies have focused on spaceborne bistatic SAR imaging algorithms under heterogeneous platforms. The signal processing of spaceborne bistatic SAR imaging mode is quite complex, involving a variety of algorithms. An et al. used a weighted fast factorized back projection (FFBP) algorithm to effectively solve the problem of azimuth ambiguity in Geosynchronous (GEO) spaceborne-airborne bistatic synthetic aperture radar (GEO-BiSAR) [7]. Li et al. reduced the phase error in spaceborne bistatic SAR by a modified bistatic range-Doppler algorithm (RDA) [8]. Wang et al. proposed a bistatic weighted BPA (BWBPA) algorithm for spaceborne bistatic SAR with a geosynchronous orbit (GEO) transmitter, which effectively suppresses azimuth ambiguity [9]. An et al. solved the problem of sub-Nyquist sampling in GEO-LEO bistatic SAR through multi-receiver technology and compressed sensing [10]. Wu et al. developed a Chirp Scaling algorithm, which successfully solved the problem of range migration in bistatic forward-looking SAR [11]. However, there is no research on the combination of modern small SAR satellites and bistatic arc array SAR. Therefore, this study explores the imaging mode and algorithms of bistatic arc array SAR with a small satellite transmitter.

AA-BiSAR with the small satellite transmitter has many advantages in imaging mode, but the special scanning of the SAR imaging system antenna, the height of modern small satellite, and high-speed motion bring about technical problems. Firstly, the high-speed motion of the satellite platform causes

* Corresponding author: Peigeng Lu (15049187096@163.com).

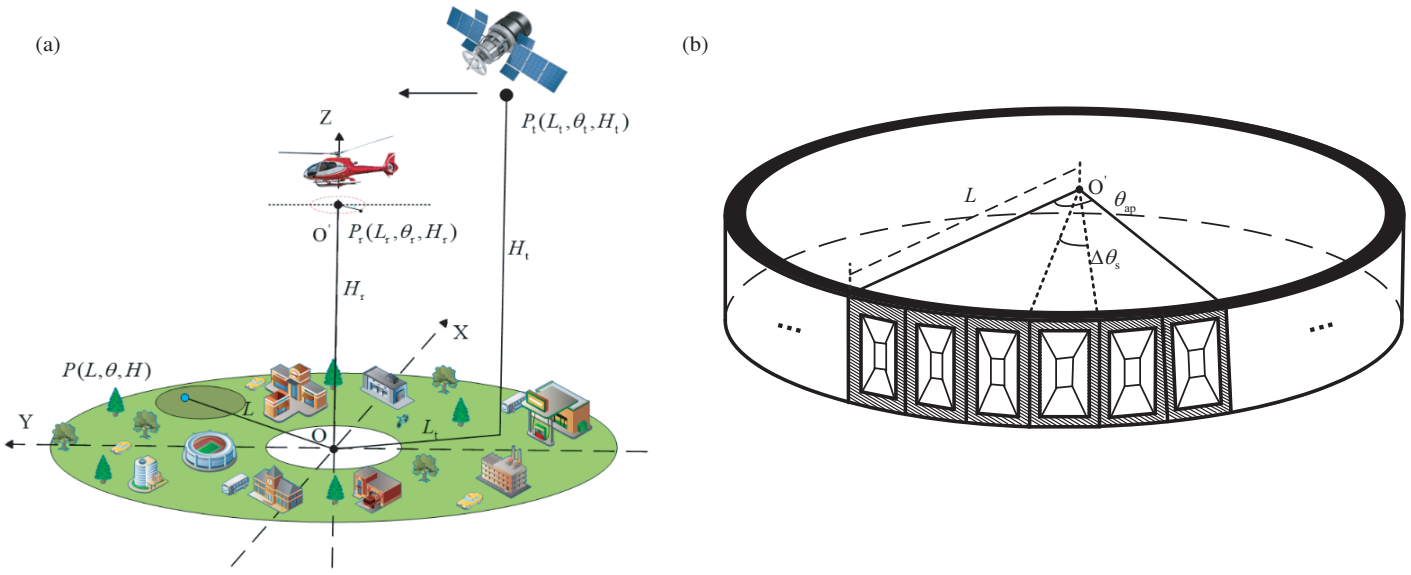

FIGURE 1. System model of AA-BiSAR with the small satellite transmitter. (a) Imaging geometry. (b) Antenna architecture.

the bistatic oblique range to be complicated and the image to be blurred and defocused. Secondly, the special scanning of arc antenna and its rotation speed lead to the coupling between range and azimuth. In order to solve these problems in the AA-BiSAR with the small satellite transmitter, an improved Chirp Scaling imaging algorithm is proposed in this paper. Firstly, the oblique range is approximated by the third-order Taylor series expansion, and then the range migration term caused by the small satellite motion is compensated by the compensation function. Then, by constructing chirp scaling (CS) function, residual range migration correction and residual phase compensation are carried out at the reference target. Finally, the effectiveness of the proposed method is verified by point target simulation experiments.

The structure of this paper is as follows. The second section describes the imaging geometry and signal model of the AA-BiSAR with the small satellite transmitter. In the third section, the imaging algorithm is analyzed. In the fourth section, the imaging analysis of the target of simulation experiment is carried out. The fifth section summarizes.

2. IMAGING GEOMETRY AND SIGNAL MODELS

2.1. Imaging Geometry

Modern small satellites have a long time in space, which can achieve large-scale coverage monitoring and communication. In order to obtain the characteristic information of the ground target effectively, a communication connection is established between the helicopter and modern small satellite. The helicopter transmits the task request signal to the modern SAR small satellite, and the small satellite transmits the radar signal to the specified scene area after receiving the signal. After the signal is reflected by the target, it is received in turn by the arc array antenna elements installed on the helicopter to complete the target imaging process. The imaging geometry model of the AA-BiSAR with the small satellite transmitter is shown in Figure 1(a). The modern small satellite moves uniformly in space with a velocity of v at an altitude of H_t, and the initial position is $P_t(L_t, \theta_t, H_t)$. L_t and θ_t are horizontal range of the satellite from the scene center and azimuth angle, respectively. The helicopter is hovering over an area at altitude H_r, equal angle sampling of the signal by the antenna, and its position is at $P_r(L_r, \theta_r, H_r)$. L_r and θ_r are antenna radius and azimuth angle of the equivalent sampling point, respectively, and its rotation angular velocity of w. The target in the ground area is located at $P(L, \theta, H)$. The height H is generally 0, and L and θ are the horizontal range from the scene center and azimuth angle, respectively. The structure diagram of the receiving antenna is shown in Figure 1(b), and the array elements are arranged successively along the arc shape to work. The antenna synthetic aperture angle is θ_{ape}. The angle interval between two antenna array elements is $\Delta\theta_{\text{sa}}$, and the number of antenna elements is N_r.

2.2. Signal Model

The echo signal expression of AA-BiSAR with small satellite transmitter is as follows:

$$s(\tau,t) = w_r\left(\tau-\frac{R_{tr}(t)}{c}\right)w_a\left(\frac{\theta_r-\theta}{\theta_a}\right)$$
$$\exp\left\{\mathrm{j}\pi k_r\left[\tau-\frac{R_{tr}(t)}{c}\right]^2\right\}\exp\left\{-\mathrm{j}2\pi\frac{R_{tr}(t)}{\lambda}\right\} \quad (1)$$

where $w_r(\cdot)$ and $w_a(\cdot)$ represent the range envelope and azimuth envelope, respectively. k_r indicates the frequency modulation. The instantaneous slant range $R_{\text{tr}}(t)$ consists of two

parts, as follows:

$$\begin{aligned} R_{tr}(t) &= R_t(t) + R_r(t) \\ &= \sqrt{\begin{array}{c}(L_t\cos\theta_t + vt - L\cos\theta)^2 \\ +(L_t\sin\theta_t - L\sin\theta)^2 + (H_t - H)^2\end{array}} \\ &+ \sqrt{\begin{array}{c}(L_r\cos\theta_r - L\cos\theta)^2 \\ +(L_r\sin\theta_r - L\sin\theta)^2 + (H_r - H)^2\end{array}} \end{aligned} \quad (2)$$

where $R_t(t)$ is the slant range from the satellite to target; $R_r(t)$ is the slant range from the equivalent sampling point to target.

Since $R_{tr}(t)$ contains the radical sign and the form of trigonometric function, Taylor series is used here for approximate expansion, and formula (2) is the approximate expansion of third-order function:

$$\begin{aligned} &R_t(t) \approx R_0 + \delta(t) \\ =&R_0 + \left(\frac{L_t\cos\theta_t - L\cos\theta}{R_0}v\right)t \\ &+\left(\frac{v^2}{2R_0} - \frac{(L_t\cos\theta_t - L\cos\theta)^2}{2R_0^3}v^2\right)t^2 \\ &-\left(\frac{(L_t\cos\theta_t - L\cos\theta)}{6R_0^3}v^2 + \frac{(L_t\cos\theta_t - L\cos\theta)}{3R_0^5}v^3\right)t^3 \end{aligned} \quad (3)$$

where $R_0 = \sqrt{L_t^2 + L^2 + H_t^2 - 2L_tL\cos(\theta_t - \theta)}$, R_0 is the instantaneous slant range of the small satellite platform at rest time; $\delta(t)$ is the oblique range component of the movement time of the small satellite platform.

The slant range $R_r(t)$ is obtained by transformation:

$$\begin{aligned} R_r(t) &\approx \sqrt{L_r^2 + L^2 + (H_r - H)^2 - 2L_rL + L_rL(\theta_r - \theta)^2} \\ &= \sqrt{R_1 + L_rL(\theta_r - \theta) + L_rLw^2t^2} \\ &= \sqrt{R_1 + L_rL(\theta_r - \theta) + v^2(L)t^2} \end{aligned} \quad (4)$$

where $v(L)$ is the speed at which the antenna rotates.

3. IMAGING PROCESSING

The range Fourier transform of echo signal $s(\tau, t)$ is carried out:

$$\begin{aligned} Ss(f_r, t) =& W_r(f_r)\, w_a\left(\frac{\theta_r - \theta_n}{\theta_a}\right) \\ &\exp\left\{-\mathrm{j}2\pi\frac{(f_c + f_r)}{c}R_{tr}(t)\right\}\exp\left(-\mathrm{j}\pi\frac{f_r^2}{k_r}\right) \end{aligned} \quad (5)$$

where f_r is the range frequency, θ_a the azimuth beamwidth, f_c the carrier frequency, and $W_r(\cdot)$ the range frequency domain envelope.

The slant range error caused by the high-speed motion of the modern small satellite platform has a certain influence on the two-dimensional (2D) space-time obtained in the imaging scene. The motion compensation function is constructed by approximating the error corresponding to the center target of the scene:

$$H_{mc}(f_r, t; R_{ref}) = \exp\left\{\mathrm{j}2\pi\frac{(f_r + f_c)}{c}\delta(t; R_{ref})\right\} \quad (6)$$

where R_{ref} is the reference range, and usually the range between the scene center target (reference point target) and the platform is chosen as the reference for motion compensation; $\delta(t; R_{ref})$ is the slant range component of the small satellite platform corresponding to the target at the center point of the scene during the movement time.

After motion compensation, the echo signal continues to carry out the inverse range Fourier transform:

$$\begin{aligned} ss_1(\tau, t) &= \mathrm{IRFFT}[Ss(f_r, t)\cdot H_{mc}(f_r, t; R_{ref})] \\ &= w_r\left(\tau - \frac{[R_r(t) + R_0]}{c}\right) w_a\left(\frac{\theta_r - \theta_n}{\theta_a}\right) \\ &\exp\left\{-\mathrm{j}2\pi\frac{[R_r(t) + R_0]}{\lambda}\right\} \\ &\exp\left[\mathrm{j}\pi k_r\left(\tau - \frac{[R_r(t) + R_0]}{c}\right)^2\right] \end{aligned} \quad (7)$$

Apply the azimuth Fourier transform to the above Equation (7), then the expression of the signal in the range Doppler domain is as follows:

$$\begin{aligned} sS_1(\tau, f_a) &= w_r\left[\tau - \left(\frac{R_0 + R_1}{c\rho(f_a, v(L))}\right)\right] W_a(f_a) \\ &\exp\left\{-\mathrm{j}2\pi\left[\frac{f_c(R_0 + R_1)\rho(f_a, v(L))}{c}\right]\right\} \\ &\exp\left\{\mathrm{j}\pi k_m\left(\tau - \frac{R_0 + R_1}{c\rho(f_a, v(L))}\right)^2\right\}\exp(-\mathrm{j}2\pi f_a t) \end{aligned} \quad (8)$$

where $\rho(f_a, v(L)) = \sqrt{1 - (f_a\cdot\lambda/2\cdot v(L))}$, $\rho(f_a, v(L))$ is the range migration factor, which affects the range change factor of SAR imaging quality, resulting in image blurring, deformation or distortion; k_m is the range modulation frequency; $k_m = 2k_rf_a^3v^2(L)\rho^3(f_a, v(L))/[2f_a^3v^2(L)\rho^3(f_a, v(L)) - k_rc(R_1 + R_0)f_a^2]$; f_a is the azimuth frequency; $W_a(\cdot)$ is the azimuth frequency envelope; c is the speed of light; τ is the range time variable; and t is the azimuth time variable.

Chirp scaling (CS) [12, 13] is an algorithm designed to adjust radar signals so that the trajectories of targets at different ranges appear consistent in imaging. This correction is achieved by introducing linear phase terms into the signal spectrum. Therefore, the CS function in the range Doppler domain is constructed:

$$H_{cs}(\tau, f_a) = \exp\left\{\mathrm{j}\pi k_mD(f_a)\left(\tau - \frac{R_{ref0} + R_{ref1}}{c\rho(f_a, v(L))}\right)\right\} \quad (9)$$

where $D(f_a)$ is the scaling factor; $R_{ref} = R_{ref0} + R_{ref1}$, R_{ref0} and R_{ref1} are the reference oblique ranges corresponding to the small satellite or helicopter to the target, respectively. $D(f_a) = 1/\rho(f_a, v(L)) - 1$, f_a is the azimuth frequency.

Formulas (8) and (9) are multiplied, and the range dimension Fourier transform is performed to obtain the 2D spectrum expression [14]:

$$\begin{aligned} &SS_1(f_r, f_a) = W_r(f_r)W_a(f_a) \\ &\exp\left[-\mathrm{j}2\pi\frac{R_{ref}}{c}\left(\frac{1}{\rho(f_a, v(R_{ref}))} - 1\right)f_r\right] \\ &\exp\left[-\mathrm{j}\frac{\pi\rho(f_a, v(R_{ref}))}{k_m}f_r^2\right] \\ &\exp\left[\mathrm{j}2\pi\frac{k_m}{c^2}(1 - \rho(f_a, v(R_{ref})))\right. \\ &\left.\left(\frac{R_0 + R_1}{\rho(f_a, v(L))} - \frac{R_{ref0} + R_{ref1}}{\rho(f_a, v(R_{ref}))}\right)^2\right] \\ &\exp(-\mathrm{j}2\pi f_a t)\exp\left(-\mathrm{j}2\pi\frac{R_0 + R_1}{c}f_r\right) \\ &\exp\left[-\mathrm{j}2\pi\frac{f_c(R_1 + R_0)\rho(f_a, v(L))}{c}\right] \end{aligned} \tag{10}$$

where the first phase term is a consistent range migration term that is not limited by the target position change, which is related to the reference slant range; the second phase term is the range modulation term after scaling processing, which has a small relationship with the range-azimuth of point target, and the reference slant range can be used for this secondary range compression (SRC). The third phase term is the residual phase after CS, which is related to the azimuth frequency and can be compensated in the azimuth direction. The fourth phase term and the fifth phase term are the linear phases of azimuth and range directions, respectively; the sixth phase term is the azimuth modulation term.

Formula (10) contains the uniform range migration term and SRC term, then the compensation function of the range dimension is:

$$\begin{aligned} &H_{rs}(f_r, f_a; R_{ref}) \\ &= \exp\left\{\mathrm{j}2\pi\frac{f_r R_{ref}}{c}\left(\frac{1}{\rho(f_a, v(r_{ref}))} - 1\right)\right\} \\ &\exp\left\{\mathrm{j}\pi\frac{\rho(f_a, v(r_{ref}))f_r^2}{k_m}\right\} \end{aligned} \tag{11}$$

Multiplying formula (10) and (11), the range migration and coupling correction in the range direction are completed, and the range inverse Fourier transform is performed to obtain the range Doppler domain signal:

$$sS_2(\tau, f_a) = \mathrm{IRFFT}\{SS_1(f_r, f_a) \cdot H_{rs}(f_r, f_a; R_{ref})\} \tag{12}$$

Formula (10) contains the azimuth modulation term and residual phase term, then the compensation function of azimuth dimension is:

$$\begin{aligned} &H_{ap}(f_r, f_a; R_{ref}) \\ &= \exp\left[-\mathrm{j}2\pi\frac{k_m}{c^2}(1 - \rho(f_a, v(R_{ref})))\right. \\ &\left.\left(\frac{R_0 + R_1}{\rho(f_a, v(L))} - \frac{R_{ref0} + R_{ref1}}{\rho(f_a, v(R_{ref}))}\right)^2\right] \\ &\exp\left[\mathrm{j}2\pi\frac{f_c(R_0 + R_1)\rho(f_a, v(L))}{c}\right] \end{aligned} \tag{13}$$

Multiplying formulas (12) and (13), the azimuth modulation is completed, and the azimuth inverse Fourier transform is performed to obtain the echo time domain signal:

$$\begin{aligned} ss(\tau, t) =& \mathrm{IAFFT}\{sS_2(f_r, f_a) \cdot H_{ap}(f_r, f_a; R_{ref})\} \\ =& w_r\left(\tau - \frac{R_0 + R_1}{c}\right)w_a\left(\frac{\theta_r - \theta}{\theta_a}\right) \end{aligned} \tag{14}$$

The flowchart of the improved CS imaging algorithm is shown in the Figure 2.

4. PROCESSING SIMULATION

In order to verify the imaging algorithm effectiveness of AA-BiSAR with a small satellite transmitter, target simulation experiments are carried out in this paper. The simulation parameters of the SAR imaging system are shown in Table 1, and the point target distribution is shown in Figure 3.

TABLE 1. Simulation parameters.

Symbol	Parameter	Value
f_c	Carrier frequency	14.5 GHz
H_t	Satellite altitude	500 km
H_r	Helicopter altitude	500 m
L_r	Antenna length	0.6 m
B_r	Signal bandwidth	900 MHz
θ_a	Beam width	80°
T_r	Scanning time	0.1 ms
Tsar	Synthetic aperture time	0.026 s

TABLE 2. Performance index analysis.

	Range		Azimuth	
	PSLR (dB)	ISLR (dB)	PSLR (dB)	ISLR (dB)
P1	−13.1522	−9.8985	−12.5047	−8.6252
P2	−13.2285	−9.9035	−12.5731	−8.7124
P3	−13.1294	−9.8607	−12.7923	−9.2778

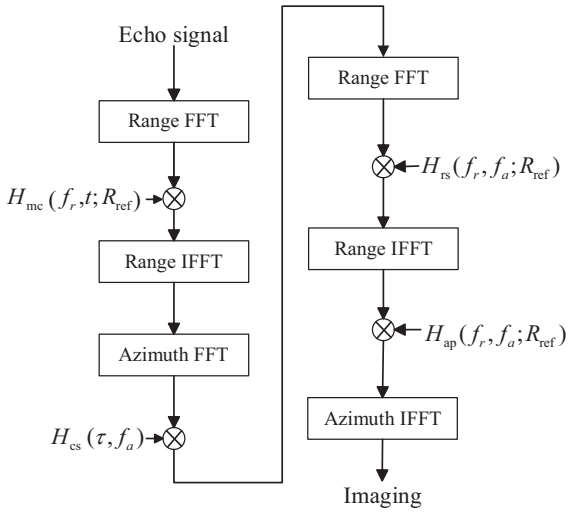

FIGURE 2. Imaging flow chart of AA-BiSAR with a small satellite transmitter.

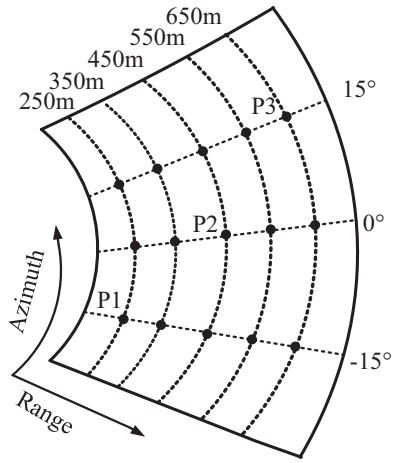

FIGURE 3. Multiple target distribution map.

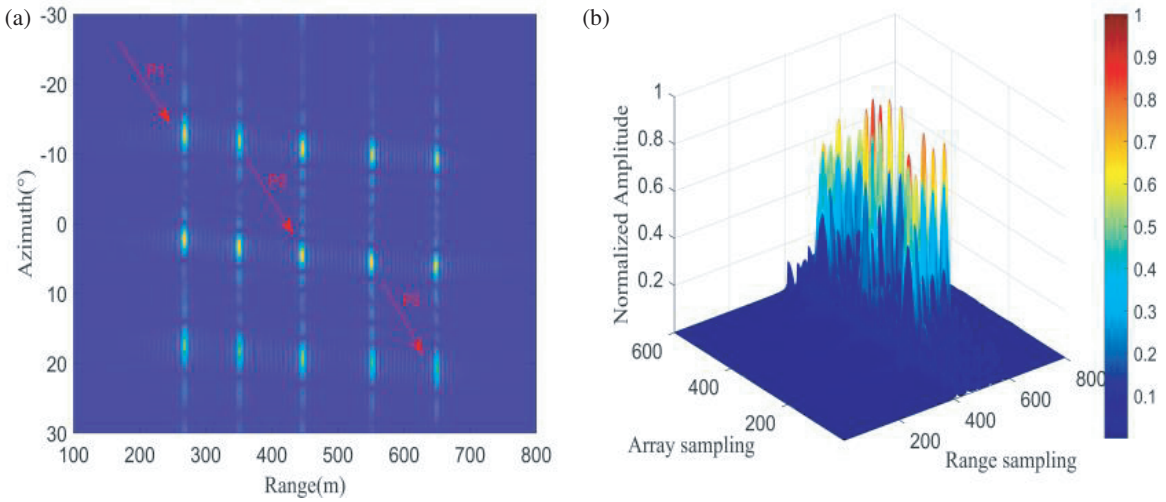

FIGURE 4. Image of multiple point targets generated using the method in Reference [11]. (a) The imaging result of multiple targets. (b) Two-dimensional cross-section of target three-dimensional imaging.

Figure 4 shows the simulation results of multiple point-targets obtained by using the conventional CS algorithm in [11]. The imaging result of multiple point-targets processed by the conventional CS imaging algorithm is shown in Figure 4(a), and the two-dimensional section of the three-dimensional point-targets is shown in Figure 4(b). The simulation result of multiple point-targets obtained by using the improved CS algorithm is shown in Figure 5(a), and the two-dimensional section of the three-dimensional point-targets is shown in Figure 5(b). It can be seen from Figure 4 that the point-target imaging results processed by the conventional CS algorithm have defocusing and blurring phenomena. In Figure 5, the point-target imaging results processed by the improved CS algorithm in this paper have a significant focusing effect; especially the imaging quality of the center point is better than that of the edge point. Compared with the two-dimensional cross section of the point-target processed by the conventional CS algorithm, the results of the improved algorithm show a better overall imaging effect. By selecting the center point P2 and remote endpoints P1 and P3 for simulation comparison, the contour maps are shown in Figures 6(a), (b), (c) and Figures 7(a), (b), (c), respectively. It can be seen that the point-targets processed by the conventional CS algorithm have trailing, offset, and defocusing phenomena, and the main lobe is coupled with the side lobe. The point-targets processed by the improved CS algorithm are separated from the main lobe and side lobe. There is no coupling phenomenon, and the focusing effect is good. In addition, three well-focused target contour maps show that the imaging quality of the central point P2 is better than that of the remote points P1 and P3. In short, the improved CS algorithm proposed in this paper significantly improves the focusing effect of point-target imaging, especially in the central point imaging quality.

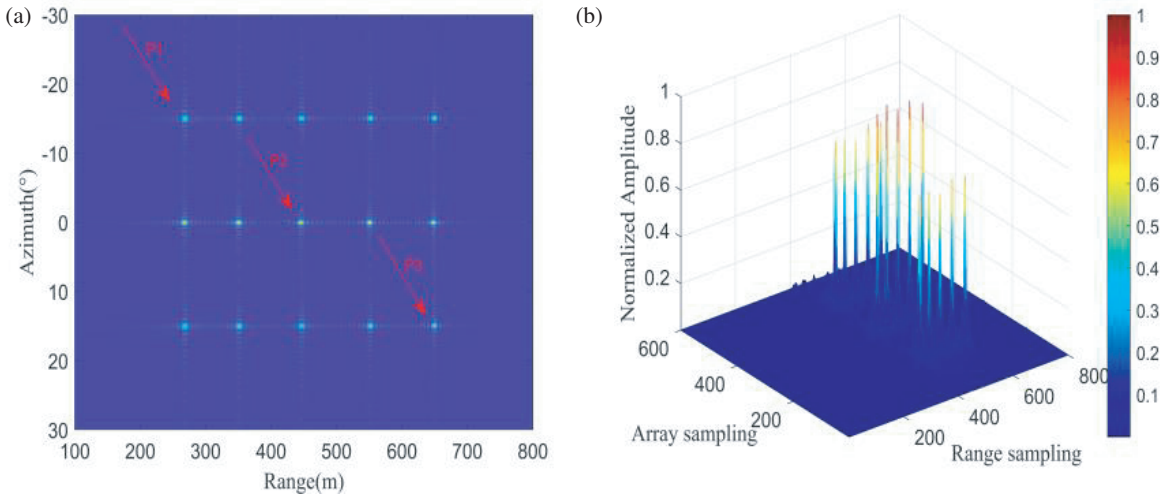

FIGURE 5. Image of multiple point targets is generated by using the method in this paper. (a) The imaging result of multiple targets. (b) Two-dimensional cross-section of target three-dimensional imaging.

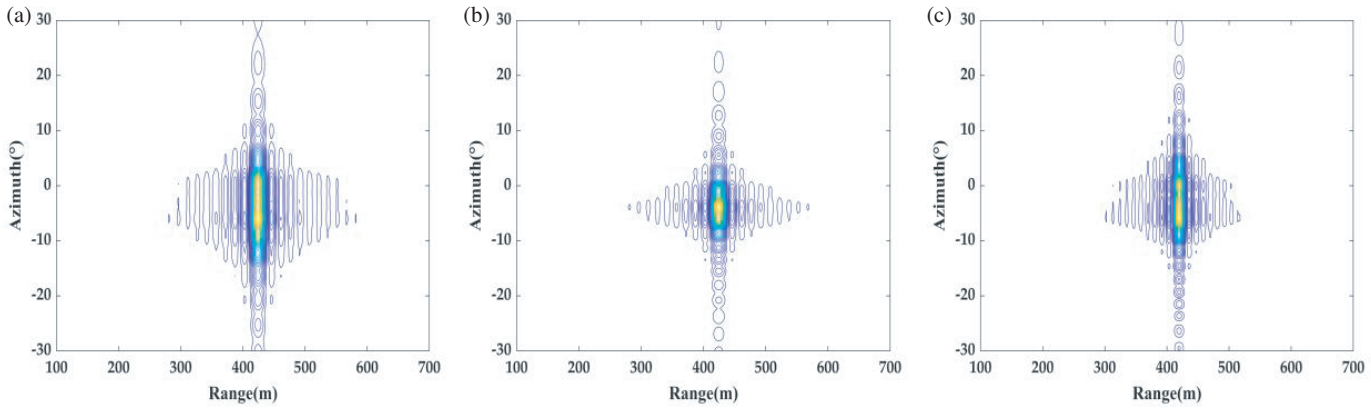

FIGURE 6. The contour plots of P1, P2, P3 generated using the method in Reference [11]. (a) The contour map of P1 target. (b) The contour map of P2 target. (c) The contour map of P3 target.

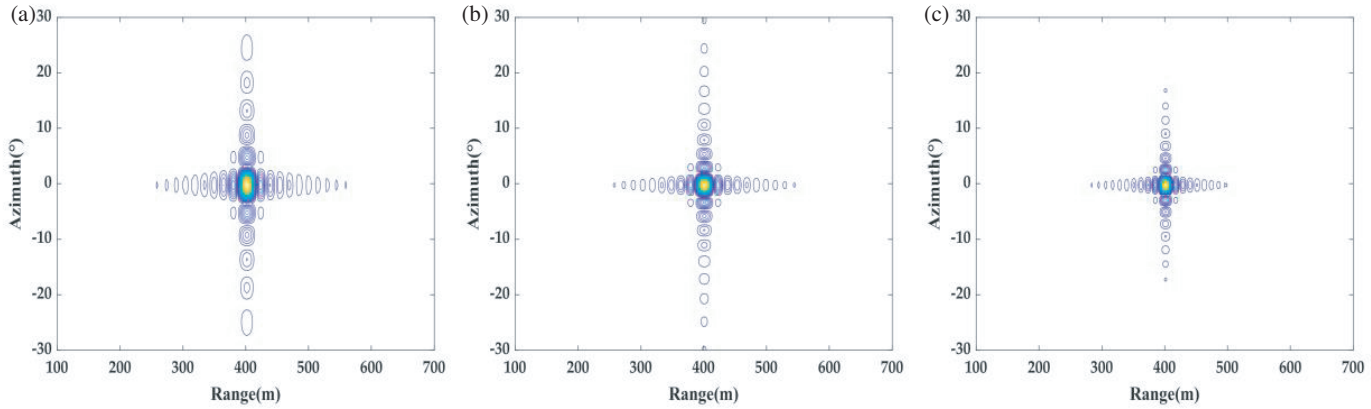

FIGURE 7. The contour plots of P1, P2, P3 are generated by using the method in this paper. (a) The contour map of P1 target. (b) The contour map of P2 target. (c) The contour map of P3 target.

The peak side lobe ratio (PSLR) and integral side lobe ratio (ISLR) of the point target are analyzed. The imaging performance analysis is shown in Table 2. As can be seen from the performance index results of the three points, the performance parameters have slightly decreased, but are still close to the theoretical value in general. It can be seen that both point targets

in the imaging scene have ideal imaging effects, which indicates that the improved CS algorithm proposed in this paper for AA-BiSAR with a small satellite transmitter is effective.

5. CONCLUSIONS

The rapid development of modern small satellites, which can serve as a transmitter to assist helicopter operations, shows the potential for cooperation between different platforms. In this paper, an imaging model of AA-BiSAR with a small satellite transmitter is studied. Based on the special structure, height and speed differences of the transmitting-receiving platform, an improved Chirp Scaling algorithm for AA-BiSAR with a small satellite transmitter is proposed. Firstly, the problem of range migration caused by the high-speed motion of small satellites is eliminated according to the idea of motion compensation. Then the residual range migration momentum of different range target-points is corrected to the same target point by scaling processing, and the coupling phase between range and azimuth is corrected by consistent range migration correction and secondary range compression in two-dimensional frequency domain. The residual phase is then eliminated in the azimuth term. Finally, the effectiveness of the proposed method is verified by target simulation results.

ACKNOWLEDGEMENT

This work was supported in part by National Natural Science Foundation of China under grant numbers 62071258 and U22A2010.

REFERENCES

[1] Bai, Z., "Development achievements and prospects of China's modern small satellite," *Spacecraft Engineering*, Vol. 28, No. 2, 1–8, 2019.

[2] Lin, L. and X. Zhang, "Modern small satellites and public space age," *Spacecraft Engineering*, Vol. 24, No. 3, 75–84, 2015.

[3] Huang, P., K. Li, W. Xu, W. Tan, Z. Gao, and Y. Li, "Focusing arc-array bistatic synthetic aperture radar data based on keystone transform," *Electronics*, Vol. 8, No. 12, 1389, 2019.

[4] Zhu, X., P. Huang, W. Xu, W. Tan, and Y. Qi, "A modified keystone-based forward-looking arc array synthetic aperture radar 3D imaging method," *Sensors*, Vol. 23, No. 5, 2674, 2023.

[5] Xiao, M., P. Huang, W. Xu, W. Tan, Z. Gao, and Y. Qi, "An airborne arc array synthetic aperture radar vibration error compensation method," *Sensors*, Vol. 24, No. 3, 1013, 2024.

[6] Huang, P., L. Hao, W. Tan, W. Xu, and Y. Qi, "An adjusted frequency-domain algorithm for arc array bistatic SAR data with one-moving transmitter," *Sensors*, Vol. 22, No. 13, 4725, 2022.

[7] An, H., J. Wu, Z. He, Z. Li, and J. Yang, "Geosynchronous spaceborne–airborne multichannel bistatic SAR imaging using weighted fast factorized backprojection method," *IEEE Geoscience and Remote Sensing Letters*, Vol. 16, No. 10, 1590–1594, 2019.

[8] Li, C., H. Zhang, Y. Deng, R. Wang, K. Liu, D. Liu, G. Jin, and Y. Zhang, "Focusing the L-band spaceborne bistatic SAR mission data using a modified RD algorithm," *IEEE Transactions on Geoscience and Remote Sensing*, Vol. 58, No. 1, 294–306, 2020.

[9] Wang, Y., Y. Liu, Z. Li, Z. Suo, C. Fang, and J. Chen, "High-resolution wide-swath imaging of spaceborne multichannel bistatic SAR with inclined geosynchronous illuminator," *IEEE Geoscience and Remote Sensing Letters*, Vol. 14, No. 12, 2380–2384, 2017.

[10] An, H., J. Wu, K. C. Teh, Z. Sun, and J. Yang, "Nonambiguous image formation for low-earth-orbit SAR with geosynchronous illumination based on multireceiving and CAMP," *IEEE Transactions on Geoscience and Remote Sensing*, Vol. 59, No. 1, 348–362, 2021.

[11] Wu, J., J. Yang, Y. Huang, and H. Yang, "Focusing bistatic forward-looking SAR using chirp scaling algorithm," in *2011 IEEE RadarCon (RADAR)*, 1036–1039, 2011.

[12] Sun, Z., W. Zhang, and S. Zhang, "An improved CS imaging algorithm for spaceborne/airborne hybrid bistatic SAR," in *Proceedings of 2011 IEEE CIE International Conference on Radar*, Vol. 2, 1489–1492, 2011.

[13] Liao, Y. and e. al., "An improved CS imaging algorithm for large scene circular scanning SAR," *Journal of Astronautics*, Vol. 37, No. 1, 127, 2016.

[14] Wu, S., C. Li, G. Yang, S. Zheng, H. Gao, M. Zhao, H. Geng, X. Liu, and G. Fang, "MIMO-SA-based 3-D image reconstruction of targets under illumination of terahertz gaussian beam — Theory and experiment," *IEEE Transactions on Microwave Theory and Techniques*, Vol. 71, No. 9, 4080–4097, 2023.